analytical chemistry

Article

High-Throughput Nanoparticle Characterization via Glow Discharge Optical Emission Spectroscopy Elemental Mapping

Kevin Finch, Aldo Hernandez, and Gerardo Gamez*

Cite This: https://doi.org/10.1021/acs.analchem.2c03940
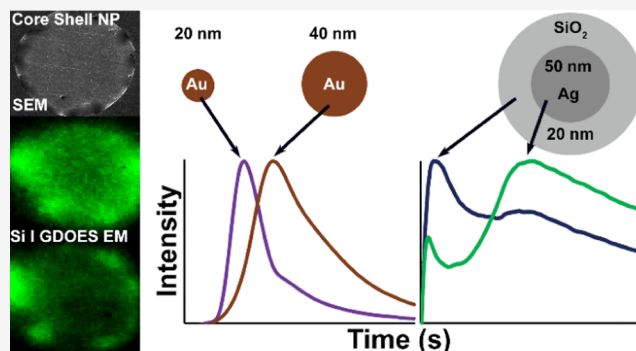
Read Online

ACCESS | Metrics & More | Article Recommendations | Supporting Information

ABSTRACT: Nanoparticle (NP) characterization is critical in many fields due to its use in numerous applications. Traditional NP characterization techniques, however, are limited by low sample throughput, and few can measure the size and elemental composition. Furthermore, sample throughput limitations are compounded in elemental mapping (EM) techniques for obtaining NP spatial distribution. Glow discharge optical emission spectroscopy (GDOES) EM can provide large area maps directly and cost-effectively from solid samples within tens of seconds. Here, GDOES EM is demonstrated for the first time for NP characterization in terms of mass, elemental composition, and size/structure dimensions. The effects of GD pulsed power, pressure, and sample substrate were studied, and optimized conditions resulted in limits of detection at single pg levels. While this is not at the level of single nanoparticle sensitivity, size differentiation of Ag and Au nanoparticles was successfully demonstrated between 5 and 100 nm, while the internal dimensions of complex core−shell NPs were also identified through the optical emission changes as a function of time.

Nanoparticles (NPs) have been gaining increased interest in the last few decades[1,2] due to their unique properties compared to their bulk material counterparts, which has resulted in their use for a wide variety of applications. The chemical composition, size, shape, charge, and surface functionalization have all been known to change their unique physical and chemical properties.[1] Due to the intensified use of NPs in many different industries, they are being found with greater prevalence in many environmental systems. Ag NPs are one of the greatest contributors to this increasing prevalence,[3] as they are one of the most marketable nanomaterials currently in use with applications ranging from textile production,[4] agriculture,[5] and improved food storage[6] to the biomedical[7] and pharmaceutical[8] fields because of their well-known antimicrobial properties.[9]

Nevertheless, the toxicity of these NPs in the environment is not currently well-understood, part of which can be attributed to the lack of high throughput, widely available, and cost-effective characterization techniques for monitoring their characteristic properties from the production stage to their integration with the environment. There are currently a variety of techniques available for the chemical identification or characterization of NPs.[2] Few techniques can yield both elemental composition and size characteristics, but while they all have their own unique advantages and disadvantages, typical methods of choice are limited in sample throughput. Some techniques allow elemental mapping (EM), e.g., electron microscopy[10−12] and X-ray techniques[10,11,13] to study NP

distribution in systems of interest, but this in turn brings more sample throughput limitations and may require hours to tens of hours for mapping large surface areas (≥ 100 cm^2). Some EM X-ray techniques for NP characterization are able to circumvent the long acquisition-time requirements through the use of synchrotron radiation, but these sources are not widely available, which also results in limited sample throughput.

Thus, alternative higher-throughput techniques are becoming available that can provide NP composition and size information. One such technique is single particle inductively coupled plasma mass spectrometry (sp-ICP-MS), which has the capability to measure particle size and particle number concentrations (PNCs) with high throughput for simple liquid matrices.[14−16] It should be noted that size determinations are constrained by single particle mass detection limits. Moreover, it has several disadvantages, as highlighted in recent efforts to minimize them,[17−19] including significantly more involved sample preparation for complex matrices, requirements for PNC below a certain threshold, operating conditions only optimum to certain NP type/solution matrix combination,[20]

assumptions on particle shape, and difficulty analyzing elements with higher background (e.g., O, H, C). Furthermore, EM is not inherent to sp-ICP-MS but is only available when coupled with laser ablation sampling, with its corresponding low sample throughput for large-scale maps.[21,22] More recently, a graphite furnace atomic absorption spectroscopy method was also demonstrated for the composition and sizing of Au NPs between 2 and 100 nm from suspensions,[23] but without EM capabilities.

Glow discharge optical emission spectroscopy (GDOES) is a high-throughput solid-sampling simultaneous multielemental analysis technique that requires little-to-no sample preparation and offers multimatrix calibration schemes.[24] GDOES also allows the analysis of light elements (O, H, C, N), where most other techniques fail.[24] Furthermore, GDOES EM has been realized through the implementation of pulsed-power schemes while maintaining the discharge at higher-than-typical pressures.[25,26] Under these conditions, the sputtered atom mixing in the discharge before emission can occur is minimized, thus preserving the lateral information with a resolution of $\sim$100 μm.[24] GDOES EM is cost-effective and several orders-of-magnitude faster than the EM techniques based on ion- or photon-beam rastering. Moreover, inherent access to depth resolution coupled to the fast sputtering rates permits three-dimensional (3D) (spatial) elemental information in rapid time frames while having the ability to measure analytes in relatively complex matrices.

Herein, GDOES EM is demonstrated for the first time for the high-throughput detection and characterization of metallic NPs from dried-droplet residue arrays. The effect of the GDOES EM operating conditions and sample preparation were studied, and optimized conditions were used for the determination of the elemental composition limit-of-detection (LOD). Furthermore, the shape of the intensity time profiles is used to show the novel ability to perform NP composition and size, as well as core−shell dimensions characterization via GDOES EM.

■ EXPERIMENTAL SECTION

Glow Discharge. The Grimm-type GD[27] chamber used in this study was modified from a version described previously.[28] Briefly, the Ar plasma gas is not evacuated through the cathode−anode gap, and the entire sample (cathode) is under vacuum, in contrast to the typical Grimm design.[27] The chamber was further adapted to permit mounting and characterization of petrographic microscope slide-type substrates (27 mm × 46 mm, 1.2 mm thickness), and the schematic is shown in Figure S1. A brass-restricting anode assembly was designed to reduce the 40 mm i.d. to 19 mm i.d., (20 mm o.d.) and extend its length toward the cathode to maintain a gap of $\sim$100 μm. A MACOR slide interface electrically isolated the anode from the cathode and was designed to accept the microscope slides. A brass backing electrode was used directly for conductive substrates. In the case of nonconductive substrates, a Cu plate (12.2 mm × 40.2 mm) embedded in a PTFE plate was used to minimize arcing to the backing electrode, which is observed in this particular GD cell design. The pressure was maintained with a gauge (MKS, Series 910), vacuum pump (Leybold, TRIVAC D-25-B), and a mass flow controller (MKS, Type 1197A Mass-Flo) at an Ar flow rate of 0.05 slpm. A 13.56 MHz RF generator (Dressler, Cesar 1350) was used to deliver RF pulses at 1 kHz and 5% or 12.5% duty cycle. The RF power was tuned via

impedance matching (Dressler, VM-5000-W) prior to each measurement and kept constant.

Imaging System. The push-broom hyperspectral imaging (PbHSI) system, described previously,[29−32] was adapted here to perform as an imaging spectrograph. Briefly, the light from the GD is demagnified $\sim$1.9× by a triplet ultraviolet−visible (UV−vis) achromat lens. An iris (field stop) was added at the focal point of the collection lens for blocking stray light originating outside the region-of-interest, resulting in an effective f-number of 14.3 for the imaging system. Then, a pair of triplet UV−vis achromat lenses collimate and refocus the image with a 90° turning mirror placed in between to steer the light into the entrance slit of the spectrograph. The entrance slit width was set to 1.5 mm to obtain (x, y, and λ) information simultaneously while preventing the need to scan in any dimension. This allows the highest imaging duty cycle without detrimental loss of the rapidly transient signal. An 1800 lines/mm grating was selected for most studies to give a spectral window of $\sim$16 nm (linear dispersion of 1.2 nm/mm), except the Ag core−silica shell characterizations (see below). A series of images was collected until the analyte was completely sputtered, and no emission was observed. Each image integrated 100 GD pulses or 10 GD pulses for select experiments together on-chip (IOC) at a frame readout of 4.78 Hz. The iCCD camera (Andor, iSTAR 334T) gate was delayed 17 μs, with either 45 or 120 μs gate width, to acquire data after 5 μs from the onset of RF pulse, at 2 × 2 pixel binning. GDOES EM time profiles are representative of the time necessary to collect each image without readout time.

Sample Preparation. All dilutions were performed with DI water. Standard NP solutions were obtained from nanoComposix, where $\bar{x}$ = average d. and σ = 1 standard deviation; poly(vinylpyrrolidone) (PVP) Ag NPs: ($\bar{x}$ = 9.7 nm, σ = 2.1 nm), ($\bar{x}$ = 51 nm, σ = 9 nm), ($\bar{x}$ = 74.1 nm, σ = 8.2 nm); Ag core−silica shell NPs: ($\bar{x}$ = 82, σ = 5 nm), ($\bar{x}$ = 126, σ = 12 nm); and citrate Ag NPs: ($\bar{x}$ = 5.4, σ = 0.8 nm). The citrate Ag NPs: ($\bar{x}$ = 10, σ = 4 nm), ($\bar{x}$ = 20, σ = 4 nm), ($\bar{x}$ = 40, σ = 4 nm), ($\bar{x}$ = 100, σ = 8) and citrate Au NPs: ($\bar{x}$ = 20, σ = 3 nm), ($\bar{x}$ = 40, σ = 4 nm), ($\bar{x}$ = 100, σ = 8) were all obtained from Sigma-Aldrich. Core−shell NP stock solutions came suspended in ethanol, while all others were in DI water. Suspensions were shaken for $\sim$30 s when removed from the refrigerator and for $\sim$15 s prior to being drop-cast manually with a volumetric pipette into three dried deposits ($\sim$2 mm d., separated by $\sim$1.5 mm edge-to-edge) distributed along a vertical line, which was aligned along the spectrograph's 13 mm slit height to permit simultaneous imaging without scanning.

Pressure, Power, and Substrate Studies. Deposits of 20 μL 40 nm Ag NPs in citrate buffer at a concentration of 20 ng/μL were drop-cast in 1 μL intervals (20×) and allowed to dry between depositions. Excessive spreading was observed on glass slides due to wetting and was restricted through the use of home-made vinyl sticker "masks." These masks had an array of holes to provide wells where the NP suspension droplets were confined into 2 mm d. deposits during the drying step and were removed prior to analysis. This protocol was also used for the Cu substrates to facilitate BEC comparisons with the glass (Figures S2A and 1C).

A dichroic filter (Andover Corp, 337FS03-25, transmission of 24.4% at 338.3 nm) was placed after the collimation lens to enable use of the iCCDs full dynamic range by minimizing the stronger wavelength bands. The iCCD gate width was 45 μs
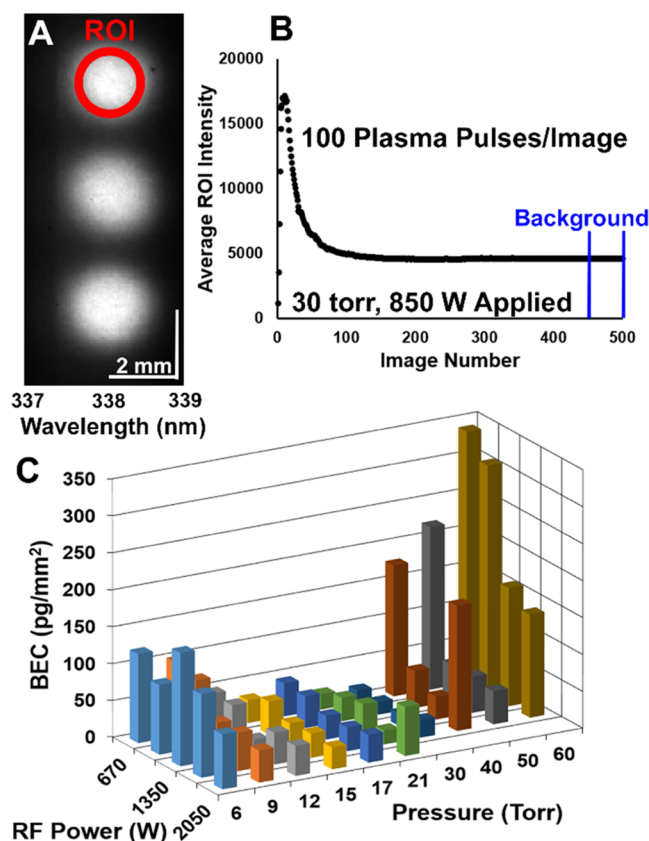
Figure 1. (A) GDOES EM at 338.28 nm (Ag I) of 3-replicate 400 ng deposits of 40 nm citrate-functionalized Ag NPs on a Cu plate. (B) Temporal profile of the signal intensity averaged within the region-of-interest (ROI) in panel A. The last 50 images were taken as background for BEC calculations. (C) BEC, normalized to deposit area, as a function of the plasma gas pressure and applied RF power.

with a plasma pulse width of 50 μs at 1 kHz pulse frequency. The RF power was tuned into the Cu substrates via impedance matching at each pressure and had a high coupling efficiency to the Ag NPs at the 400 ng deposited mass without using longer plasma pulse widths. 1 image = 100 plasma pulse IOC. Averaged time traces were created using ImageJ and defining a circular ROI with an edge threshold equal to 50% of the spectrally subtracted peak height. The ROI was then averaged over all pixels within this area to give an average intensity value as a function of time. The intensity values of 3-replicate deposits on one substrate were then averaged together to provide an averaged time trace. BECs were calculated using the peak height as the signal, and the last 50 images (where no Ag signal was observed) of each averaged time trace were used to obtain the mean and standard deviation of the background. LODs were calculated using 3× the standard deviation of the y-intercept divided by the slope.

Limit-of-Detection Determination. The vinyl mask protocol was not implemented to prevent any potential loss of NPs that may be deposited on the edges of the vinyl. The dichroic filter was also removed to provide higher signal-to-noise (S/N) ratios since the filter rejects about 75% of light at the Ag I wavelength. The 40 nm citrate-functionalized Ag NPs were used with 5 replicate volume deposits of 0.25 μL each (1.25 μL total) at decreasing concentrations, 20 − 0.16 ng/μL, resulting in a mass of 25 ng − 200 pg for each final dried sample. The 50 nm PVP-functionalized Ag NPs were prepared

the same way as the citrate, with the addition of a 0.04 ng/μL suspension, which resulted in a 50 pg dried sample for the lowest mass. The iCCD gate width was 120 μs, with a corresponding plasma pulse width of 125 μs at 1 kHz pulse frequency. The RF power was tuned via impedance matching at every mass and was necessary due to lower coupling efficiency at lower masses. 1 image = 100 plasma pulses IOC. Nine deposits (3 slides) were averaged together for statistics.

The images were binned 5 × 5 in software, resulting in an image with 10 × 10 binning total. The four highest intensity pixels were then chosen as the ROI for averaging the signal, which corresponded to an actual deposit area of 494 × 494 μm after the image magnification was taken into account. The PNC (per unit area) at various masses for both citrate and PVP-functionalized Ag NPs were then counted manually in each SEM image (Center and Edge of ROI) and averaged together to extrapolate the mass of NPs in the ROI (Table S1). A linear calibration curve was created between the total deposited mass and ROI mass, with the SEM mass corrected values used for the calibration curves. LODs were calculated using 3× the standard deviation of the y-intercept divided by the slope. The LOD error reported was propagated from the standard deviation of the slope.

Nanoparticle Size Characterization. The size determination experiments for both PVP- and citrate-functionalized Ag or Au NPs used five replicate volume deposits at 0.25 μL each (20 ng/μL concentration) to result in a total mass of 25 ng (1.25 μL) deposited for all of the d. (5−100 nm). The iCCD/plasma conditions and the data analysis procedure were the same as for the LOD determination studies. For the PVP Ag NP sizing studies, the larger masses of the citrate Ag NPs (20−100 nm), and the Au NPs 100 plasma pulses were integrated on-chip for a single image. In the case of the smaller-sized citrate Ag NPs (5−20 nm), 10 plasma pulses integrated on-chip for a single image. An intensity time trace was created from nine replicate measurements (three substrates with three deposits each) and was used to obtain the FWHM/FW75%M and peak time statistics. Time traces were filtered in time using MATLAB with the function "sgolayfilt" using a third-order polynomial with an 11-pixel (image) window.

Silver Core/Silica Shell Nanoparticle Characterization. The characterization of the Ag core−silica shell NPs used five replicate volume deposits at 5 μL each (20 ng/μL concentration) to result in a total mass of 50 ng (2.5 μL) for both sizes. The Ag I (328 nm) and Si I (251.6 nm) emissions were monitored simultaneously using the 300 lines/mm grating, resulting in a spectral window of ∼130 nm at a linear dispersion of 9.8 nm/mm. The iCCD gate width was 120 μs with a corresponding plasma pulse width of 125 μs (12.5% duty cycle@1 kHz pulse frequency). The silica shells of both the 90 and 140 nm d. NPs had 20 nm thick shells, and the core sizes were 50 and 100 nm, respectively.

The ROI for each core−shell image was selected at the edges of each deposit, and the high spatial resolution provided by the GDOES EM images allows discrimination of emission signals, where emission time profiles align temporally and have similar peak intensities. These characteristics are indicative of regions where the particle density and sputtering rate are similar. Nine of these time traces (three substrates with three deposits each) are then chosen to average together. Time traces were filtered in time using MATLAB with the function "sgolayfilt" using a third-order polynomial with an 11-pixel (image) window.

283 The SEM images (pristine vs sputtered 15 s) were analyzed
284 in ImageJ using the "analyze particles" function. Parameters
285 used were: "Auto Local Threshold" with method "Niblack" and
286 a 15-pixel radius, size "100−750 pixels," a circularity of "0.35−
287 1," and "include holes." The data obtained was then used in
288 Matlab with the function "histogram" and "normalization" was
289 set to "probability" to plot size distributions. The "histfit"
290 function was then used to fit Poisson distributions to the
291 individual histograms and obtain lambda and standard
292 deviation values.

293 ### ■ RESULTS AND DISCUSSION

294 **Effect of GD Pressure and Power.** The GDOES spectral
295 image at 338.28 nm under EM conditions (Figure 1A) shows
296 the discrete emission from each Ag NP deposit. The average
297 pixel intensity from the region-of-interest (ROI) changes from
298 image-to-image, as a function of time, showing a peak at image
299 ∼8 and decreases to a plateau as the sample is consumed by
300 sputtering (Figure 1B). The effect of the GD applied power
301 and gas pressure on the Ag I emission was assessed by
302 calculating the background equivalent concentration (BEC =
303 $(0.01 \times k \times RSDB \times C0) \times SBR\text{-}1$),[33] which serves as an
304 indicator of the LOD, where k=3, RSDB is the relative
305 standard deviation of the background, C0 is the deposit total
306 mass of silver, and SBR is the peak signal-to-background ratio.
307 The BEC here is also normalized to the deposit area to account
308 for the signal intensities spread over the iCCD pixels. It is
309 evident that the BEC considerably improves (decreases) from
310 6 Torr up to 30 Torr. The lateral resolution in GDOES EM is
311 known to improve at higher pressures,[34] but signal intensities
312 typically decrease. Thus, the unexpected BEC improvement
313 trend observed here, resulting from comparable corresponding
314 improvements in peak S/B and RSDB (Figure S3), is
315 significantly advantageous. The trend is hypothesized to be
316 caused by a lateral plasma confinement effect (PCE) on the
317 NP deposit due to the higher sputtering rate of NPs[35,36] vs the
318 bulk substrate material on which they are deposited. The PCE
319 will become more significant at higher pressures due to the
320 plasma constriction that takes place from an increasingly lower
321 mean free path.[24] The PCE will lead to higher power density
322 not only at the NP deposit but also at higher lateral resolution,
323 which will result in higher analyte signal and lower background
324 from the bulk substrate, thus yielding lower LODs.
325 Furthermore, the BEC becomes worse (increases) as the
326 pressure is further increased from 30 to 60 Torr (Figure 1C)
327 due to the instability of the plasma. It is worth noting that this
328 is the first time GDOES EM is demonstrated above 12 Torr for
329 quantitative purposes.[34,37] In addition, the BEC generally
330 improves as the RF power is increased. The optimum
331 conditions at 30 Torr and 850 W applied power (WA) were
332 subsequently used for the rest of this study.

333 **Effect of the Substrate Material.** The effect of the bulk
334 substrate composition on the figures-of-merit was also studied.
335 Particular attention was paid to the substrate's relative
336 sputtering rate (RSR), since it would potentially affect the
337 hypothesized PCE.

338 As such, glass petrographic slides, characterized by a low
339 RSR as a thick nonconductive substrate, were tested. While the
340 BEC here (Figure S2A) followed a similar pressure trend as the
341 Cu plate substrate, the pressure could not be raised ≥15 Torr
342 due to arcing issues arising from the whole nonconductive
343 substrate being entirely in vacuum. Lateral resolution is much
344 better at 30 vs 12 Torr, so only conductive substrates were

345 further investigated. However, the typical Grimm[27] GDOES
346 sample mount should prevent such issues and will be tested in
347 the future.

348 The effect of conductive substrate RSR on the LOD of Ag
349 NPs was evaluated via mass-calibration curves (Figure S2B).
350 Evidently, as the substrate RSR decreases, so does the
351 corresponding LOD (Table 1). These results support the

Table 1. Relative Sputtering Rates of Metallic Substrates and Corresponding LODs from Mass-Calibration Curves

	Cu	Ni	Ti
RSR mean	3.5	1.5	0.43
full deposit LOD (pg)	674	412	134

352 proposed PCE because the higher NP/substrate RSR contrast
353 would enhance plasma confinement. The simple drop-casting
354 NP deposition method was also optimized. Drop-casting is
355 known to produce a distinct "coffee-ring" stain of higher
356 particle density at the perimeter,[38] which is clearly observed
357 here for the single-drop deposition protocol (1 × 1.25 μL)
358 images under the optical (Figure 2A) and electron microscopes
359 (Figure 2B). The spatial resolution of GDOES EM (Figure
360 2D) also allows us to clearly observe this effect. In addition,
361 SEM shows how the PNC significantly increases from the
362 center of the deposit outward (Figure 2C,E,F). The "coffee-
363 ring" effect was minimized here by implementing a drop-
364 casting technique with five replicate deposit volumes (5 × 0.25
365 μL). The five-drop technique allowed not only a more
366 homogeneous NP distribution over the deposit but also
367 depositing the same mass onto a significantly smaller area, ∼4×
368 (c.f. Figure 2A,B, and 1D vs 2G,H,J, note different scales). The
369 SEM identified a much thicker ring (c.f. Figure 2B,H) and
370 increased PNC toward the center of the deposit in comparison
371 to the single-drop deposit (c.f. Figure 2E,F,K,L). The higher
372 mass/area in the five-drop method, which was used for the rest
373 of this study, will also result in better SNR.

374 **Limit-of-Detection.** Quantitative figures-of-merit with the
375 optimized conditions were obtained for Ag NPs with different
376 surface functionalization, citrate vs PVP, from calibration
377 curves (Figure 3A,B). In this case, the ROI was restricted to
378 the center of deposit (∼0.5 radius), enabled by the high
379 GDOES EM spatial resolution achieved in our study by
380 operating at 30 Torr. The spatial resolution at 30 Torr was
381 calculated using the line-spread function[39] from the vertical
382 edges of three deposits (six edges) and was found to be
383 between ∼130 and ∼160 μm. SEM of the ROI confirmed that
384 no NP stacking was taking place, such that the sub-monolayer
385 thickness is limited by the NP diameter. In addition, the PNC
386 distribution obtained by SEM in the ROE allowed to use only
387 the corresponding NP mass, instead of the NP mass of the
388 whole deposit. Variations in the measured V_{DC} between
389 replicates were observed and were subsequently used to
390 normalize the peak intensities of each image, which led to a
391 significantly better linearity and reproducibility. It is worth
392 noting that the GD power pulse duration was set to 50 μs for
393 citrate Ag NPs, while it was 125 μs for PVP Ag NPs.

394 The longer pulse duration improved reproducibility but
395 resulted in higher background intensity, which is reflected as a
396 curvature in the linear function toward the lower masses
397 (Figure 3) due to displaying the data on a log scale and having
398 a nonzero y-intercept. Nevertheless, comparable LODs were
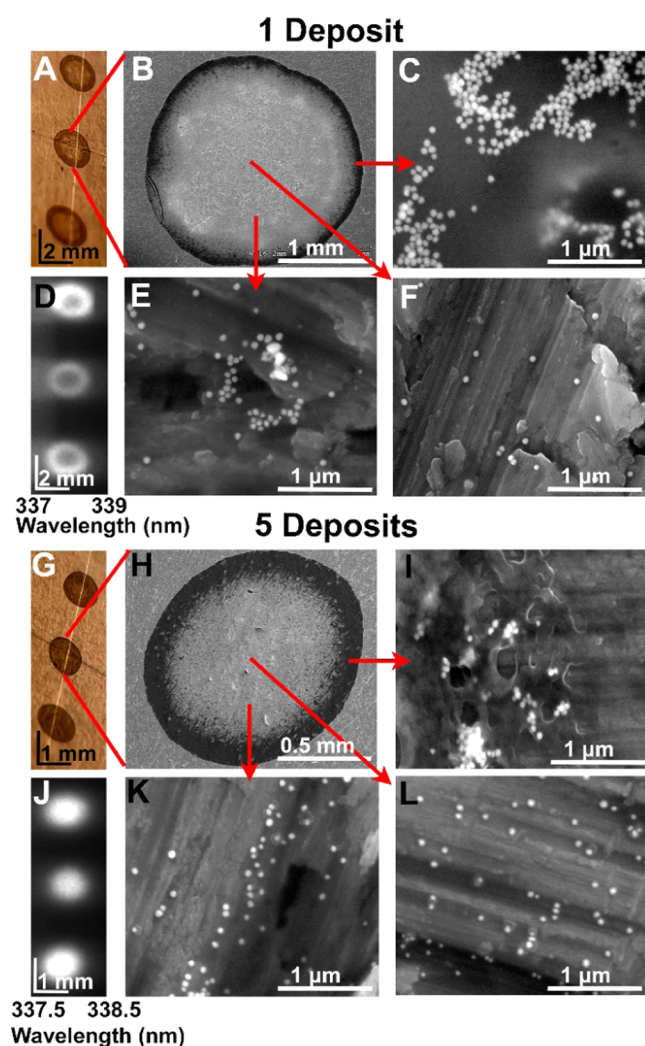399 obtained for 40 nm citrate Ag NPs (3 ± 0.01 pg or 2.4 pg/μL,

Figure 2. Single 1.25 μL sample, 25 ng total of 40 nm citrate Ag NPs, drop-cast per deposit on Cu substrate, as observed by optical microscopy (A), SEM at different magnifications (B, C, E, F), and measured by GDOES EM using MIS mode at 338 nm wavelength (D, Ag I). Five 0.25 μL replicate samples, 25 ng total of 40 nm citrate-functionalized Ag NPs, drop-cast per deposit on Cu substrate, as observed by optical microscopy (G), SEM at different magnifications (H, I, K, L), and measured by GDOES EM using MIS mode at 338 nm wavelength (J, Ag I). Note the differences in the scale bars between A, B, D vs G, H, J.

Figure 3. Calibration curves of the GDOES EM NP deposit ROI average peak intensity (20 × 20 pixel binning, showed for three replicate 25 ng deposits) normalized to the V_{DC} vs NP mass for Citrate 40 nm Ag NPs (A) and PVP 50 nm Ag NPs (B). Error bars: standard deviation of nine replicate measurements. (C) SEM of the full 25 ng PVP deposit (left) and the center (right).

Figure 3A) and 50 nm PVP Ag NPs (8 ± 0.04 pg or 6.4 pg/μL, Figure 3B). This is due in great part to using the measured ROI mass for calibration, which allows us to account for differences in PNC distribution between citrate and PVP (cf. Figures 2L and 3C), which was significantly higher for PVP in the ROI. The mass LODs can be put into perspective by considering a study monitoring the uptake of 50 nm citrate Ag NPs into mouse neuroblastoma single-cells by laser ablation ICP-MS, which reported an average mass uptake of 81 ± 67 pg/cell[40] and LODs of 157 pg/μL.[40] Thus, the GDOES EM Ag NP LODs shown here are appropriate for single-cell uptake studies, with the caveat that these LODs were demonstrated on standard Ag NP solutions, and single-cell matrix effects are yet to be investigated. Future work by the authors will include studying the effects from cellular matrices to assess GDOES EM applicability. It is also important to assess the effect of having ionic species present in the matrix with NPs, as is

common with real-world samples. When 25 ng of AgNO$_3$ (5 × 0.25 μL@20 ng/μL) was analyzed using the same method as the PVP Ag NPs, no Ag signal was observed. However, when 25 ng of AgNO$_3$ was added to 25 ng of Ag NPs, the signal was seen to increase by ~21% in comparison to the NP suspension by itself. This can be explained by the NPs allowing more efficient plasma coupling into the sample through the previously mentioned PCE. Nevertheless, concentrations of ionic Ag found in environmental water systems (rivers, lakes, and estuaries) are on the order of ~10−100 ng/L, which are 5−6 orders-of-magnitude lower than what was measured in this study;[41] thus, ion contributions to the total signal will not be significant.

Nanoparticle Size Characterization. Next, the ability to perform NP size characterization via GDOES EM was also
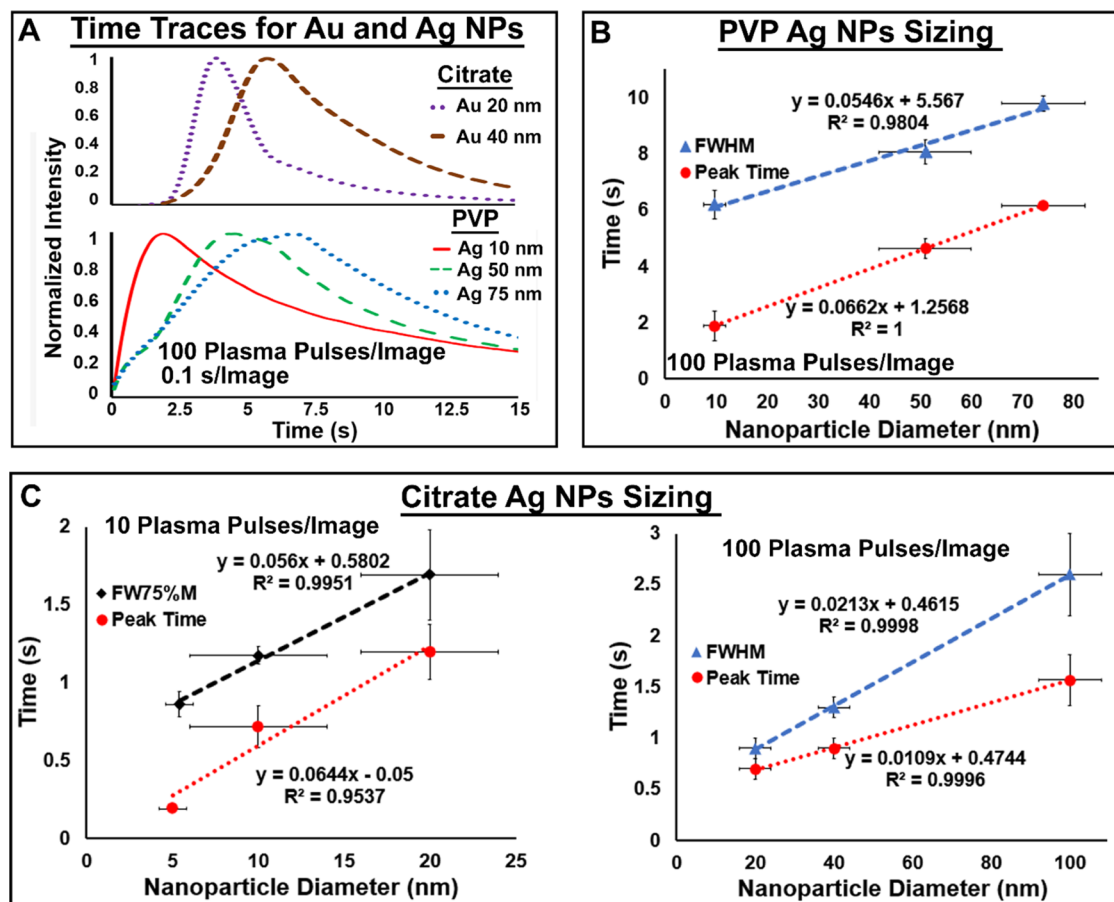
Figure 4. (A) Optical emission intensity time profiles of 25 ng deposits of PVP Ag NPs and citrate Au NPs. Calibration plots of time profiles FWHM (or FW75%M) and peak time vs PVP Ag NP d. (B), as well as 25 ng deposits of citrate Ag NPs at a small NP d. range (C left) and large NP d. range (C right). *X*-error bars: standard deviations from manufacturers' certificate of analysis. *Y*-error bars: standard deviation for nine replicate measurements. Note the difference in the plasma pulses/image between the citrate Ag NPs sizing plots.

studied. The emission time profiles show that the peak intensity occurs at a later time and the full width at half-maximum (FWHM) becomes wider as the NP d. in the deposit is increased in the range of 10−100 nm (Figure 4). Both effects show a linear relationship, even with different NP surface functionalization, which is greatly due to the sub-monolayer thickness corresponding to the NP d. Decreasing ×10 the number of plasma pulses accumulated per image allowed the time resolution necessary to lower the NP d. range to 5−20 nm (Figure 4C). In this case, the full width at 75% of the maximum (FW75%M) had to be used because of the emission time profile tailing. The FWHM/FW75%M and peak time NP d. analytical sensitivities generally improve for larger d. (Table S2). To the authors' knowledge, this is the first time GDOES, in any operation mode, is demonstrated for the characterization of NP size. Differentiation of Au NPs with d. of ∼20 vs ∼40 nm, with sharper time profile peaks and minimal tailing, demonstrates that this technique is also applicable to various NP compositions (Figure 4A).

It is noteworthy that the FWHM/peak times are different for the citrate vs PVP-coated Ag NPs (cf. Figure 4B,C). Thus, it would indicate that these calibration curves are specific to an NPs surface coating, such that prior separation based on their functionalities[42−45] would need to be implemented to use this method as is. Alternatively, a universal calibration curve could be achieved by removing the capping agents by simple washing/centrifugation, other chemical methods,[46−48] or "soft"

plasma cleaning,[49] which is a unique possibility with GD, as demonstrated for the removal of organic surface contaminants.

Ag Core/Silica Shell Nanoparticle Characterization. Finally, the capability of GDOES EM to characterize internal dimensions of complex NPs was also studied with Ag core/silica shell NPs. The emission time profiles for ∼90 nm total d. ($\bar{x}$ = 47 nm, σ = 5 nm core) and 140 nm total d. ($\bar{x}$ = 92 nm, σ = 12 nm core) show clear discrimination in peak times between the Si and Ag signals (Figure 5A,B). It can be seen that the Si I signal peaks first at ∼2−3 s for both NP sizes, while the Ag I peaks later at 15 s for the 90 nm NPs or 18 s for the 140 nm particles. This shows that the silica shell is sputtered first before exposing the Ag core, which is consistent with a layer-by-layer sputtering process. This allows the ROI to be located at the edge of the deposit despite NP agglomerating on top of each other. The SEM images of the core/shell NP sample sputtered to the Ag I peak show smaller core sizes compared to the ones in the pristine sample. Some NPs in the sputtered sample SEM also appear hollow, which is believed to be due to the high sputtering rate differences between SiO_2 and Ag; once the core has been exposed to the plasma, the Ag may be sputtered away more rapidly, while the silica shell remains and acts to block core edges from incoming sputtering species. The core size distribution histogram (Figure 5D) shows the overall core size shifts to smaller d., as confirmed by Poisson fits (Figure 5E), giving a λ = 46.37 nm/standard deviation = 6.8 for the pristine sample, and λ = 43.51 nm/
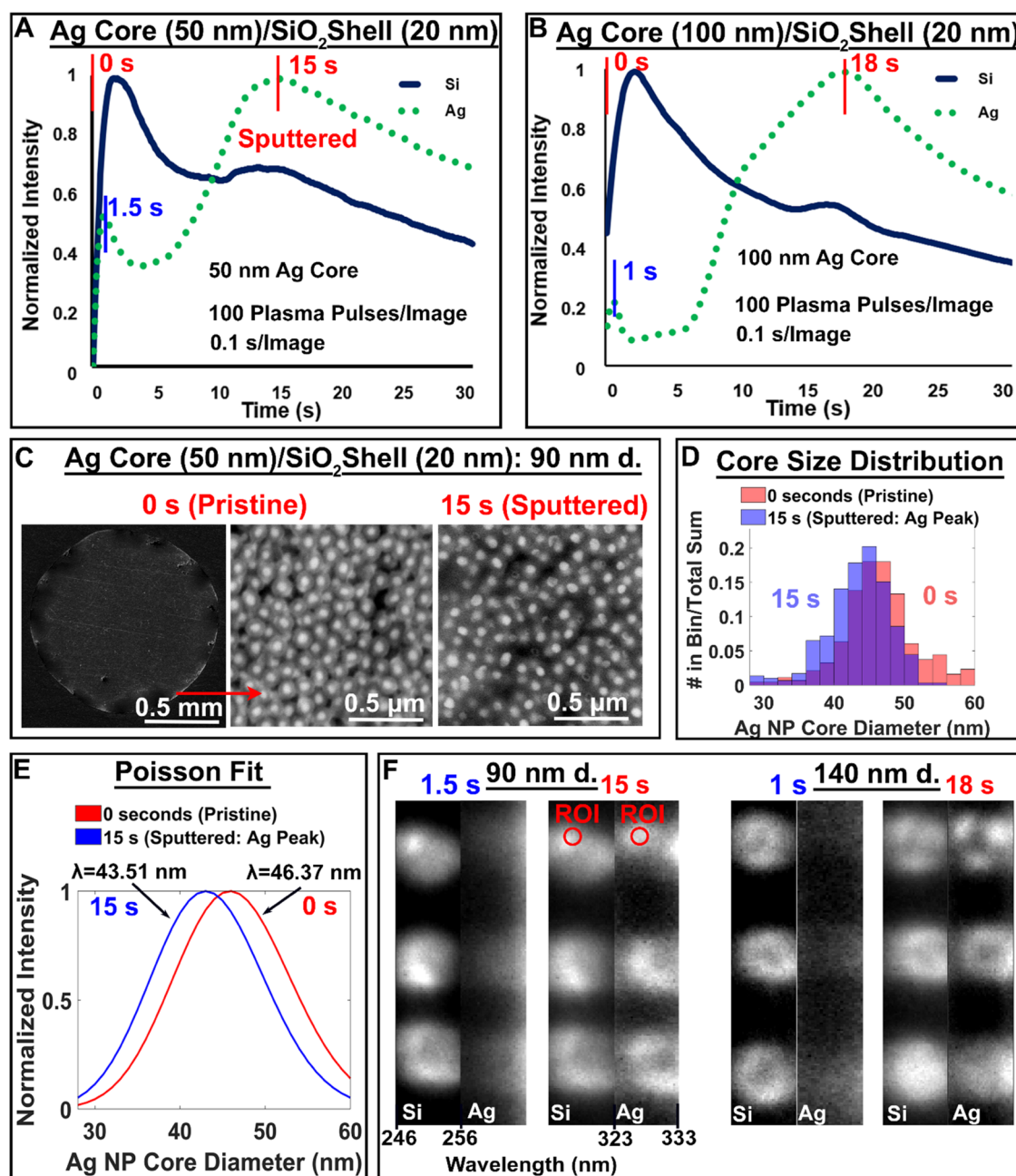
Figure 5. Optical emission intensity time profiles of 50 ng Ag core/SiO$_2$ shell NPs: (A) 90 nm total d., Ag core ($\overline{x}$ = 47 nm, σ = 5 nm). (B) 140 nm total d., Ag core ($\overline{x}$ = 92 nm, σ = 12 nm). (C) SEM images of the 90 nm total d. deposit before sputtering/pristine and after sputtering to the Ag I peak time. (D) Histogram of NP core size distribution from SEM images (overlap is shown in purple) and corresponding (E) Poisson fits. (F) GDOES EM images at various times along the time profile for both Si I (251 nm) and Ag I (328.1 nm).

standard deviation = 6.6 for the sputtered sample. The pristine sample SEM measured core d. are in good agreement with the manufacturers' specifications of 47 ± 5 nm, which was measured via TEM.

Furthermore, it should be noted that, in this case, the larger spectral window used to measure Si I and Ag I simultaneously has a lower spectral resolution. Thus, background subtraction is less efficient, particularly for the Ag I lines with N$_2$ bands in the vicinity, and results in artifacts on its time profile shape, such as the residual initial peak at ∼1 s (Figure 5A,B). The GDOES EM images (Figure 5F) at the corresponding background residual peak in Figure 5A (1.5 s) and 5B (1 s) show only molecular interferences at adjacent wavelengths overlapping the Ag wavelength. In addition, there are no characteristic spatial features indicative of emission from the NPs deposit, such as in the GDOES EM images at the Ag I peak time for 90 nm (15 s) and 140 nm (18 s) core−shell particle sizes. On the other hand, sputtering rates and plasma impedance matching vary between material "layers," and here, the impedance matching settings were kept constant throughout the measurement (see the Experimental Section). Thus, the second peak in the Si I time profile, which coincides with Ag I, may be a result of improved impedance matching/ sputtering rate as the Ag core is exposed. Current work in the authors' laboratory is underway to develop faster hyperspectral imaging approaches with the higher spectral resolution, such as

coded aperture snapshot spectral imaging (CASSI) coupled with GDOES EM to allow significantly better simultaneous multielemental capabilities with improved background subtraction (NSF: CHE-2108359).

CONCLUSIONS

In conclusion, this is the first time GDOES, in any operation mode, has been demonstrated for the successful discrimination of NP sizes and their elemental composition. GDOES EM enables significantly faster (data collection within seconds) NP characterization, with information about their spatial distribution over relatively large area samples, in comparison to traditional techniques. Furthermore, GDOES EM is also shown to give access to core/shell NP composition and structure dimensions. It is worth noting that size determinations are not constrained by single particle mass detection limits. Moreover, this technique requires very fast and simple sample preparation without specialized equipment. Nonetheless, better deposition methods that can deposit more NPs, up to a full monolayer, in a smaller area could provide better mass LODs from the correspondingly higher signal density and improved SBR. Future work will include analysis of mixtures containing various NP sizes to assess the possibility of differentiation based on their temporal profiles. In addition, the technique presented opens the door for developing many different applications in several fields currently underway in the authors' laboratory, such as cell NP uptake studies down to the single cell, analysis of NPs in microarray platforms for even orders-of-magnitude higher-throughput analysis, and coupling with relevant NP separation techniques (e.g., gel electrophoresis[42,45]/thin layer chromatography[43,44,50]) for more comprehensive characterization.

Current work is also underway to adapt this method to typical GDOES operating conditions, or GDMS, which may lack EM capabilities but are widely accessible in commercially available instruments and would allow access to composition analysis and even size characterization with other sample deposition methods that yield more homogeneous monolayer NP distribution. Nonetheless, core−shell dimensions characterization is not subject to the requirement of a monolayer and thus could be directly applied.

ASSOCIATED CONTENT

Ⓢ Supporting Information

The Supporting Information is available free of charge at https://pubs.acs.org/doi/10.1021/acs.analchem.2c03940.

Schematic of GD chamber; plot of Peak S/B trends, substrate optimization curves; mass calculation in analyzed ROI; and analytical sensitivities for sizing (PDF)

AUTHOR INFORMATION

Corresponding Author

Gerardo Gamez − *Department of Chemistry and Biochemistry, Texas Tech University, Lubbock, Texas 79409-1061, United States;* ⃝ orcid.org/0000-0002-8827-6647;
Email: gerardo.gamez@ttu.edu

Authors

Kevin Finch − *Department of Chemistry and Biochemistry, Texas Tech University, Lubbock, Texas 79409-1061, United States*

Aldo Hernandez − *Department of Chemistry and Biochemistry, Texas Tech University, Lubbock, Texas 79409-1061, United States*

Complete contact information is available at:
https://pubs.acs.org/10.1021/acs.analchem.2c03940

Notes

The authors declare no competing financial interest.

REFERENCES

(1) Hosokawa, M. *Nanoparticle Technology Handbook*, 2nd ed.; Elsevier: Amsterdam Boston, 2012.

(2) Ing, V. D. H.; Wolfgang, U.; Alex, S. *Characterization of Nanoparticles: Measurement Processes for Nanoparticles*; Elsevier: Amsterdam, 2020.

(3) Yu, S.-j.; Yin, Y.-g.; Liu, J.-f. *Environ. Sci.: Processes Impacts* **2013**, *15*, 78−92.

(4) Chen, C.-Y.; Chiang, C.-L. *Mater. Lett.* **2008**, *62*, 3607−3609.

(5) Nair, R.; Varghese, S. H.; Nair, B. G.; Maekawa, T.; Yoshida, Y.; Kumar, D. S. *Plant Sci.* **2010**, *179*, 154−163.

(6) Rhim, J.-W.; Park, H.-M.; Ha, C.-S. *Prog. Polym. Sci.* **2013**, *38*, 1629−1652.

(7) Shenava, A.; Sharma, S.; Shetty, V.; Shenoy, S. *J. Oral Res. Rev.* **2015**, *7*, 35−38.

(8) Neupane, N. P.; Kushwaha, A. K.; Karn, A. K.; Khalilullah, H.; Khan, M. M. U.; Kaushik, A.; Verma, A. *Biocatal. Agric. Biotechnol.* **2022**, *39*, No. 102229.

(9) León-Silva, S.; Fernández-Luqueño, F.; López-Valdez, F. *Water, Air, Soil Pollut.* **2016**, *227*, No. 306.

(10) Hodoroaba, V. D.; Rades, S.; Salge, T.; Mielke, J.; Ortel, E.; Schmidt, R. *IOP Conf. Ser.: Mater. Sci. Eng.* **2016**, *109*, No. 012006.

(11) Rades, S.; Hodoroaba, V.-D.; Salge, T.; Wirth, T.; Lobera, M. P.; Labrador, R. H.; Natte, K.; Behnke, T.; Gross, T.; Unger, W. E. S. *RSC Adv.* **2014**, *4*, 49577−49587.

(12) Crouzier, L.; Delvallée, A.; Ducourtieux, S.; Devoille, L.; Tromas, C.; Feltin, N. *Ultramicroscopy.* **2019**, *207*, No. 112847.

(13) Holder, C. F.; Schaak, R. E. *ACS Nano* **2019**, *13*, 7359−7365.

(14) Mitrano, D. M.; Lesher, E. K.; Bednar, A.; Monserud, J.; Higgins, C. P.; Ranville, J. F. *Environ. Toxicol. Chem.* **2012**, *31*, 115−121.

(15) Degueldre, C.; Favarger, P. Y. *Colloids Surf., A* **2003**, *217*, 137−142.

(16) Laborda, F.; Bolea, E.; Jiménez-Lamana, J. *Anal. Chem.* **2014**, *86*, 2270−2278.

(17) Hendriks, L.; Ramkorun-Schmidt, B.; Gundlach-Graham, A.; Koch, J.; Grass, R. N.; Jakubowski, N.; Günther, D. *J. Anal. At. Spectrom.* **2019**, *34*, 716−728.

(18) Gundlach-Graham, A.; Mehrabi, K. *J. Anal. At. Spectrom.* **2020**, *35*, 1727−1739.

(19) Tanner, S. D. *J. Anal. At. Spectrom.* **1995**, *10*, 905−921.

(20) Tan, S. H.; Horlick, G. *J. Anal. At. Spectrom.* **1987**, *2*, 745−763.

(21) Li, Q.; Wang, Z.; Mo, J.; Zhang, G.; Chen, Y.; Huang, C. *Sci. Rep.* **2017**, *7*, No. 2965.

(22) Metarapi, D.; van Elteren, J. T.; Šala, M.; Vogel-Mikuš, K.; Arčon, I.; Šelih, V. S.; Kolar, M.; Hočevar, S. B. *Environ. Sci.: Nano* **2021**, *8*, 647−656.

(23) Leopold, K.; Brandt, A.; Tarren, H. *J. Anal. At. Spectrom.* **2017**, *32*, 723−730.

(24) Gamez, G.; Finch, K. *Spectrochim. Acta, Part B* **2018**, *148*, 129−136.

(25) Gamez, G.; Voronov, M.; Ray, S.; Hoffmann, V.; Hieftje, G.; Michler, J. *Spectrochim. Acta, Part B* **2012**, *70*, 1−9.

(26) Webb, M. R.; Hoffmann, V.; Hieftje, G. M. *Spectrochim. Acta, Part B* **2006**, *61*, 1279−1284.

(27) Grimm, W. *Naturwissenschaften* **1967**, *54*, 586.

(28) Voronov, M.; Hoffmann, V.; Steingrobe, T.; Buscher, W.; Engelhard, C.; Storey, A. P.; Ray, S. J.; Hieftje, G. M. *Plasma Sources Sci Technol.* **2014**, *23*, No. 054009.

(29) Shi, S.; Gong, X.; Mu, Y.; Finch, K.; Gamez, G. *J. Anal. At. Spectrom.* **2018**, *33*, 1745−1752.

(30) Kroschk, M.; Usala, J.; Addesso, T.; Gamez, G. *J. Anal. At. Spectrom.* **2016**, *31*, 163−170.

(31) Shi, S.; Finch, K.; She, Y.; Gamez, G. *J. Anal. At. Spectrom.* **2020**, *35*, 117−125.

(32) Shi, S.; Finch, K.; Gamez, G. *J. Anal. At. Spectrom.* **2021**, *36*, 1055−1073.

(33) Boumans, P. W. J. M.; Ivaldi, J. C.; Slavin, W. *Spectrochim. Acta, Part B* **1991**, *46*, 641−665.

(34) Gamez, G.; Ray, S. J.; Andrade, F. J.; Webb, M. R.; Hieftje, G. M. *Anal. Chem.* **2007**, *79*, 1317−1326.

(35) Sigmund, P. Sputtering by Ion Bombardment Theoretical Concepts. In *Sputtering by Particle Bombardment I: Physical Sputtering of Single-Element Solids*; Behrisch, R., Ed.; Springer: Berlin Heidelberg: Berlin, Heidelberg, 1981; pp 9−71.

(36) Jiménez-Sáez, J. C.; Pérez-Martín, A. M. C.; Jiménez-Rodríguez, J. J. *Nucl. Instrum. Methods Phys. Res., Sect. B* **2013**, *316*, 210−214.

(37) Gamez, G.; Mohanty, G.; Michler, J. *J. Anal. At. Spectrom.* **2013**, *28*, 1016−1023.

(38) Mampallil, D.; Eral, H. B. *Adv. Colloid Interface Sci.* **2018**, *252*, 38−54.

(39) Finch, K.; Hernandez, A.; She, Y.; Shi, S.; Gamez, G. *J. Anal. At. Spectrom.* **2020**, *35*, 1932−1946.

(40) Hsiao, I. L.; Bierkandt, F. S.; Reichardt, P.; Luch, A.; Huang, Y.-J.; Jakubowski, N.; Tentschert, J.; Haase, A. *J. Nanobiotechnol.* **2016**, *14*, No. 50.

(41) Ratte, H. T. *Environ. Toxicol. Chem.* **1999**, *18*, 89−108.

(42) Hanauer, M.; Pierrat, S.; Zins, I.; Lotz, A.; Sönnichsen, C. *Nano Lett.* **2007**, *7*, 2881−2885.

(43) Yan, N.; Zhu, Z.; He, D.; Jin, L.; Zheng, H.; Hu, S. *Sci. Rep.* **2016**, *6*, No. 24577.

(44) Wang, Y.; Olesik, S. V. *Anal. Chem.* **2018**, *90*, 2662−2670.

(45) Jimenez, M. S.; Luque-Alled, J. M.; Gomez, T.; Castillo, J. R. *Electrophoresis* **2016**, *37*, 1376−1383.

(46) La Spina, R.; Spampinato, V.; Gilliland, D.; Ojea-Jimenez, I.; Ceccone, G. *Biointerphases* **2017**, *12*, No. 031003.

(47) Niu, Z.; Li, Y. *Chem. Mater.* **2014**, *26*, 72−83.

(48) Koczkur, K. M.; Mourdikoudis, S.; Polavarapu, L.; Skrabalak, S. E. *Dalton Trans.* **2015**, *44*, 17883−17905.

(49) Molchan, I. S.; Thompson, G. E.; Skeldon, P.; Trigoulet, N.; Chapon, P.; Tempez, A.; Malherbe, J.; Lobo Revilla, L.; Bordel, N.; Belenguer, P.; Nelis, T.; Zahri, A.; Therese, L.; Guillot, P.; Ganciu, M.; Michler, J.; Hohl, M. *J. Anal. At. Spectrom.* **2009**, *24*, 734−741.

(50) Yan, N.; Zhu, Z.; Jin, L.; Guo, W.; Gan, Y.; Hu, S. *Anal Chem.* **2015**, *87*, 6079−6087.